Exp Fluids (2009) 46:823–833
DOI 10.1007/s00348-008-0586-1

RESEARCH ARTICLE

The influence of airfoil kinematics on the formation of leading-edge vortices in bio-inspired flight

David Rival · Tim Prangemeier · Cameron Tropea

Received: 8 July 2008 / Revised: 30 September 2008 / Accepted: 21 October 2008 / Published online: 23 November 2008

Abstract The formation process of leading-edge vortices has been investigated experimentally using Particle Image Velocimetry. Various airfoil kinematics have been tested, including asymmetric and peak-shifted plunging motions, and are evaluated for $Re = 30{,}000$ and a reduced frequency range of $0.2 \leq k \leq 0.33$. By measuring the growth in the leading-edge vortex during the dynamic-stall process, the vortex pinch-off process is examined based on the concept of an optimal vortex formation time. The various kinematics are then evaluated with respect to their associated vortex strength, timing and convection into the wake.

1 Introduction

Both natural and biomimetic flight occur predominantly at low Reynolds numbers. Mueller and Batill (1982) have shown that performance at these scales is strongly hampered by the separation-prone nature of the laminar boundary layer. Contrary to classical aerodynamics, separation becomes the norm, not the exception. Such a fundamental limitation to the aerodynamics suggests that lift must be generated through unsteady aerodynamic mechanisms such as dynamic stall, as described by McCroskey (1982), where the formation and delayed convection of a leading-edge vortex (LEV) over the downstroke can be very advantageous to lift production. This aerodynamic mechanism with regard to bio-inspired flight has been examined in detail by Ellington (1999). To date it has not yet been conclusively shown that a spanwise flow is an absolute requirement in the stabilization of the LEV. One recent study by Thomas et al. (2004) demonstrated that dragonflies produce large, quasi two-dimensional LEVs over their downstroke in cruise-flight conditions. More abstract investigations into LEV formation have been performed by Panda and Zaman (1994) and Ohmi et al. (1990) for pitching and pitching/plunging airfoils, respectively. Based on these aforementioned investigations and the inspiration from natural flight, an examination into the LEV formation process for low reduced frequencies ($0.2 \leq k \leq 0.33$) and for the quasi two-dimensional case has been performed. One major objective of this study is to better understand to what extent, if at all, the LEV can be stabilized without the help of spanwise flow.

D. Rival (✉) · T. Prangemeier · C. Tropea
Institute of Fluid Mechanics and Aerodynamics,
Technische Universität Darmstadt, Darmstadt, Germany
e-mail: rival@aero.tu-darmstadt.de

2 Background

2.1 History effects

The reduced frequency in this study is defined in the following manner:

$$k = \frac{\pi f c}{U_\infty}, \tag{1}$$

where f is the plunging frequency, c the airfoil chord and U_∞ the freestream velocity. Thus for the value of $k = 0.25$ used in this study, a particle of fluid moving at U_∞ would convect $x/c \approx 12.5$ over one full period of the plunging motion. Panda and Zaman (1994) have shown that the actual convection speed (u_{conv}) of shed vortices varies between

$$0.6 < \frac{u_{\text{conv}}}{U_\infty} < 0.8 \tag{2}$$

in the vicinity of the airfoil, largely dependent on the position, size and strength of the vortex. These vortices then rapidly accelerate to the freestream velocity in the immediate wake. Therefore one can infer that a LEV shed at the bottom of the plunge stroke would travel $x/c \approx 6.25$ in the time that the airfoil would require to return back to the top of the stroke. This relatively large spacing between the LEVs suggests that the history effects in the dynamic-stall process are not strongly influenced by the previous cycle's shed vortices in the wake. Rather the history effects are expected to be more strongly influenced by the slow time scales associated with boundary-layer separation and reattachment present in the dynamic-stall process itself. In other words the state of the boundary-layer at the top of the stroke, just before the LEV formation process begins, should play a much larger role than the LEV shed from the previous cycle. A further discussion on these history effects is treated in Sect. 4.2. Measurement and comparison of these history effects are then presented in Sect. 5.2.

2.2 Optimal vortex formation

The dimensionless vortex formation time $\hat{T}$, often referred to as simply the formation time, is a measure of the state of development of a vortex. A forthcoming review paper from Dabiri (2009) suggests a level of universality among all unsteady vortical flows through the concept of an optimal vortex formation number, where the vortex stops entraining fluid from the shear layer and pinches off at a value of $\hat{T} \approx 4$. The formation time is defined in its general form in the following manner:

$$\hat{T} = \frac{C\Gamma}{D\Delta U}, \tag{3}$$

where C is a constant factor depending on the physical configuration of the vortex generator, Γ is the instantaneous vortex strength, D the characteristic length scale and ΔU the shear-layer feeding velocity. For the specific case of a two-dimensional plunging airfoil with only one LEV shed per cycle, the vortex generator constant has been set to $C = 1$ and the limiting length scale of the forming vortex set as $D = 2c$. The shear-layer feeding velocity was approximated by $\Delta U = 2\pi f h_o$, being the maximum plunge velocity of the airfoil leading edge over the downstroke. Milano and Gharib (2005) showed that maximum lift on a pitching and plunging plate was generated when $\hat{T} \approx 4$, such that the LEV would pinch off just at the end of the half stroke. A follow-up study using a translating low-aspect-ratio plate with a start-up motion was performed by Ringuette et al. (2007) to better understand the impact of the tip vortex in the start-up process. Again the LEV was found to pinch off at around $\hat{T} \approx 4$. This universal behavior in the formation of the LEV is a focus of this investigation, with close attention being given to the influence of the airfoil kinematics on this pinch-off process.

3 Experimental setup

The airfoil used in this study is the asymmetric SD7003 profile developed for transitional Reynolds numbers. The profile has a maximum thickness of approximately $0.09c$ and is rotated about the $x = c/4$ position. An attractive feature of the SD7003 profile is the substantial experimental database available in the open literature for the steady case provided in Selig et al. (1995) and Ol et al. (2005) as well as the unsteady case found in Nerger et al. (2003) and Lian et al. (2008).

The experimental rig consists of a base structure, a set of linear-motors connected with each other via a linkage system and a carbon-fibre SD7003 wall-spanning profile weighing 306 g. The profile has a chord length of 120 mm and a span of 450 mm. The profile-tip spacing at the walls is less than 2 mm on either side. Maximum static blockage in the test-section based on the frontal area was under 3%. The tunnel itself has a contraction ratio of 24:1 with five turbulence filters in the settling chamber, thus producing turbulence levels under 0.5% at these low tunnel speeds. A schematic of the test rig integrated into the Eiffel-type wind tunnel test-section at the Institute of Fluid Mechanics and Aerodynamics (TU Darmstadt) is shown in Fig. 1. The various components of the Particle Image Velocimetry (PIV) system are also included in the schematic.

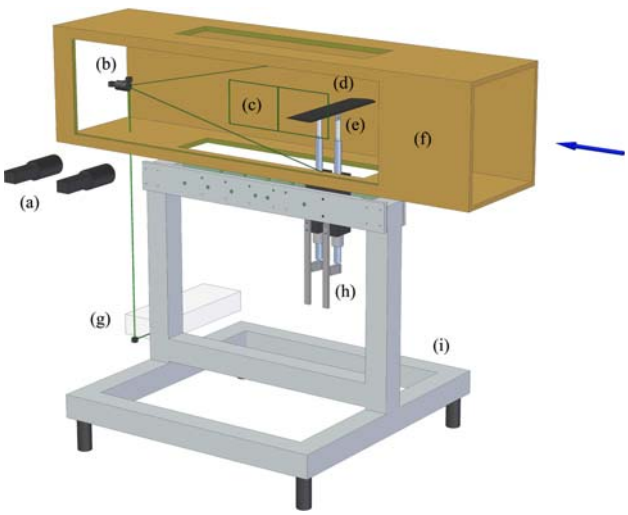

Fig. 1 Experimental setup in wind tunnel with flow direction from right-to-left: **a** CCD cameras, **b** beam expander, **c** PIV image frames, **d** wall-spanning carbon-fibre profile, **e** embedded piezo-electric force sensors, **f** test-section, **g** laser head, **h** linear motors with linkage system and **i** base structure

For the direct-force measurements a pair of one-component Kistler 9217A piezo-electric force sensors are integrated directly below the profile, one at the quarter-chord position (point of rotation) and one at the trailing edge. Together, the two sensors can measure both the profile's inertial and aerodynamic forces during the prescribed movement. The total static tare weight of the system (profile and linkage combined) totals 394 g. The analog output-charge signals from the two piezo-electric force sensors are sent through the wind-tunnel floor to a Kistler 5073A411 charge amplifier, which in turn converts the signals into an analog voltage. These voltage signals were subsequently fed into a 16-bit National Instruments 6259 A/D board. The signals are finally run through a 10 Hz low-pass filter in LabView 8.2 and are then further post-processed using MatLab 7.3.

A commercial PIV system was used in this study (Dantec Dynamics A/S) and consisted of a Nd:YAG ($\lambda = 532$ nm) Litron dual-cavity laser with a maximum power output of 135 mJ per cavity and two 10-bit FlowSense 2M CCD cameras each with a 1,600 × 1,200 pix resolution. Due to the large imaging field required, 60 mm *f*/2.8 Nikkor lenses were used. In order to reduce reflections, the profile was painted mat-black and monochromatic filters, with a corresponding wavelength of $\lambda = 532$ nm, were installed on the lenses. The laser beam was directed over three mirrors into the test-section and expanded into a sheet approximately 2 mm in thickness. This laser sheet was set parallel to the flow direction and aligned onto the airfoil quarter-span position. Due to the large imaging area of 0.0864 m^2 the laser power was set to 90% for both cavities. With the use of compressed air driven through four Laskin nozzles, DEHS seeding particles less than 1 μm in diameter were introduced into the settling chamber using a vertical rake aligned with the measurement plane.

PIV image pairs were sampled at 15 Hz allowing for 6 phases to be recorded per cycle at $k = 0.25$. In order to construct the ensemble velocity fields of 12 phases per cycle, two staggered sets with 100 images per phase were ensemble-averaged. In all cases, the first two starting cycles were removed from all ensembles. Each camera imaged a field corresponding to $x/c = 2$ and $y/c = 1.5$, with a resolution of 800 pix/*c* (6.7 pix/mm). Reflections on the model surface were strongest at the bottom of the stroke where a region 0.04*c* normal to the airfoil surface were deemed to be unreliable. Shadows and strong reflections on the pressure (lower) side required masking. Parallax effects were strongest at the top of the stroke and at this position were responsible for hiding a region 0.03*c* normal to the airfoil surface. The vector fields were calculated using an adaptive correlation with 32 × 32 pix interrogation windows and a 50% overlap. A 3 × 3 filter was used to lightly smooth the vector fields in order to more clearly define the vortical structures in the wake. The accuracy of the vector fields was estimated to lie within 2% for all cases.

Table 1 Characteristics of various test cases

Name	$f_{(downstroke)}$ (Hz)	$f_{(upstroke)}$ (Hz)	α_{eff_max} (°)	t/T (α_{eff_max})
Sinusoidal	2.5	2.5	22.1	0.25
Asymmetric	3.3	2.0	26.5	0.19
Peak-shifted	2.5	2.5	24.2	0.33
Fast-sinusoidal	3.3	3.3	26.5	0.25

4 Parameter space

4.1 Kinematics

In order to understand the effect of the airfoil kinematics on the development of the LEV, three simple and distinct

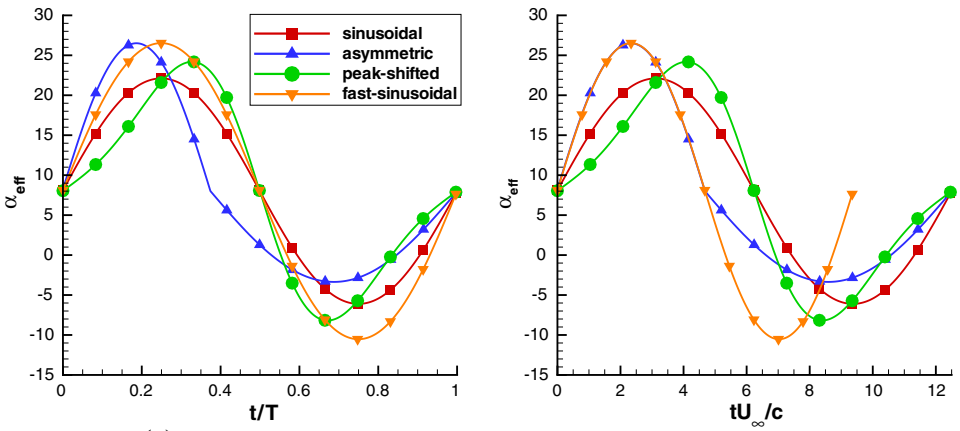

(a) with respect to period **(b)** with respect to time

Fig. 2 Effective angle-of-attack distribution for the four test cases as a function of **a** period and **b** dimensionless time; note *symbols* represent 12 measurement phases over the period

plunging motions with a constant geometric angle of attack of $\alpha_o = 8°$ and $k = 0.25$ (based on the full cycle) were selected. This incidence and frequency were chosen since they produced a well-defined LEV-TEV pair over the downstroke, as described in Rival and Tropea (2009). Once in the wake, this vortex pair has been referred to as a *mushroom-wake* structure by Panda and Zaman (1994) due to its mushroom-head shape. The plunge position (h) of the *sinusoidal* (reference) and *asymmetric* cases is based on a simple harmonic motion:

$$h(t) = h_o \cos(2\pi ft), \tag{4}$$

whereby the latter case consists of a concatenation of a fast downstroke and a slow upstroke. The *peak-shifted* case refers to a motion where the maximum plunge velocity ($\dot{h}$) and therefore the effective angle of attack (α_{eff}) occur late in the downstroke:

$$h(t) = a_1 h_o \cos\left(a_2 \sin(\pi ft) + \frac{\pi}{2}\right) - a_3, \tag{5}$$

where a_1 and a_3 are coefficients used to normalize the amplitude of the motion and $a_2 = 0.81$ is used to set the peak velocity at $t/T = 0.33$. A fourth case with $k = 0.33$ and a sinusoidal motion corresponding to the *asymmetric* downstroke was performed to access the impact of the history effects from the previous cycle. This case is referred to as the *fast-sinusoidal* case and also maintained a constant geometric angle of attack of $\alpha_o = 8°$. All cases shared a relatively large plunge amplitude of $h_o = 0.5c$. For a detailed description of the various test cases see Table 1. In Fig. 2, the variations of α_{eff} over the cycle and as a function of dimensionless time are presented for sake of clarity.

4.2 Circulatory and non-circulatory decomposition

Despite the constraints of a fully-attached flow, a planar wake and the fulfillment of the Kutta condition in classic unsteady aerodynamic theory, developed independently by Theodorsen (1935) and Kuessner (1936), such traditional models can nevertheless be useful in the estimation of the maximum attainable lift in the dynamic-stall process. At these reduced frequencies the LEV formation process is associated with a closed separation and a planar wake, and thus the basic constraints of such theoretical models are not violated. The following equation from Theodorsen decomposes the lift variation based on the assumption of superposition of the non-circulatory (added-mass) and circulatory components:

$$C_l = \frac{\pi c}{2}\left(\frac{\dot{\alpha}}{U_\infty} + \frac{\ddot{h}}{U_\infty} + \frac{c}{4}\frac{\ddot{\alpha}}{U_\infty^2}\right) + 2\pi C(k)\left(\alpha + \frac{\dot{h}}{U_\infty} + \frac{c}{2}\frac{\dot{\alpha}}{U_\infty}\right), \tag{6}$$

where a complex-valued transfer function referred to as Theodorsen's function $C(k)$ is placed in front of the circulatory component to account for the influence of the shed vorticity in the wake. All terms associated with pitching, i.e. α, $\dot{\alpha}$ and $\ddot{\alpha}$ are based on a rotation about the $c/4$ position. For the case of a pure-plunging airfoil, these pitching terms vanish leaving:

$$C_l = \frac{\pi c}{2}\frac{\ddot{h}}{U_\infty} + 2\pi C(k)\frac{\dot{h}}{U_\infty}. \tag{7}$$

In Fig. 3, the various contributions to the total lift as a function of cycle period and effective angle of attack are plotted for the reference sinusoidal case. Included in these plots are the quasi-steady curves ($2\pi\alpha$) as well as the static lift measurements from the experiment. A maximum lift of approximately $C_l \approx 1.9$ based on Theodorsen's model would be theoretically attainable if the dynamic stall process could be sustained long enough over the downstroke, i.e. the LEV would be shed at the bottom of the stroke. This is likely a reasonable estimate since it takes into consideration the negative influence of the shed

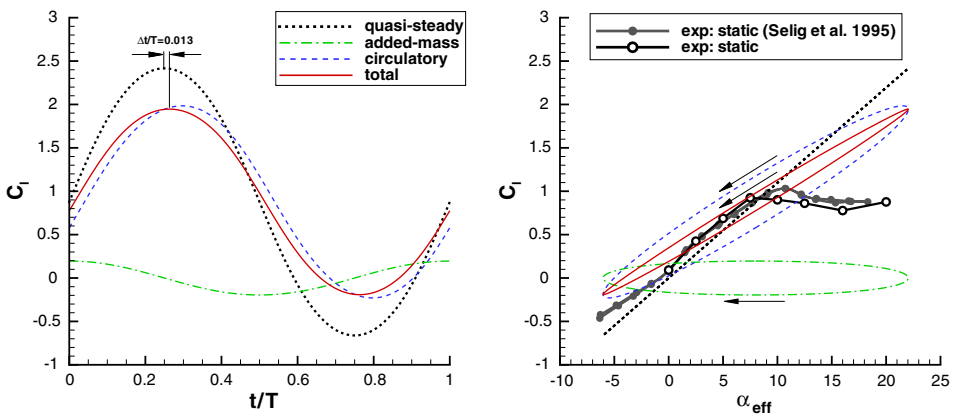

(a) with respect to period **(b)** with respect to effective angle of attack

Fig. 3 Contributions of the non-circulatory (added-mass) and circulatory components to the total lift of the sinusoidal reference case based on classical theory developed by Theodorsen (1935)

vorticity at the trailing edge (circulatory component) during the climb to the lift peak. From Fig. 3a, one can infer a time lag between the peak of the quasi-steady lift and the peak predicted from Theodorsen theory of $t/T = 0.013$, corresponding to a phase lag of $\varphi = 4.7°$. At higher reduced frequencies the added-mass contribution grows, further canceling out the aerodynamic lag imposed by the circulatory contribution. However, with the onset of a fully-stalled flow after peak lift (dynamic stall), the lift variation is found to lag dramatically behind with values as high as $\varphi = 90°$, where the relatively slow viscous time scales of the boundary-layer separation and reattachment dominate the history effects from one period to the next. This phenomenon has been clearly demonstrated using force measurements at lower reduced frequencies of $0.05 \leq k \leq 0.1$, as described in Rival and Tropea (2009).

Therefore, it becomes clear that Theodorsen's circulatory approach, which assumes attached flow, is not appropriate to predict the lift variation beyond the dynamic-stall process once the airfoil is fully stalled. However, there is no immediate reason to discount the insight provided by the non-circulatory contribution. In order to test its validity, a set of so-called *added-mass* measurements were performed. In order to measure this non-circulatory component, a dummy aluminum cylinder (shown in Fig. 4), 12 mm in diameter and identical to the SD7003 profile in mass and spanwise distribution, was constructed and mounted at the airfoil center-of-mass position in the wind tunnel test-section. With the wind tunnel turned off, sinusoidal plunge motions at various mean angles of attack were measured, both for the profile and the dummy airfoil (cylinder). The measurements were based on an ensemble of 35 cycles, sampled at 1 kHz, where the first four cycles as well as the last cycle were cut away in order to remove starting and stopping effects. By taking the difference between the airfoil and cylinder force measurements, the so-called added-mass contribution could be obtained.

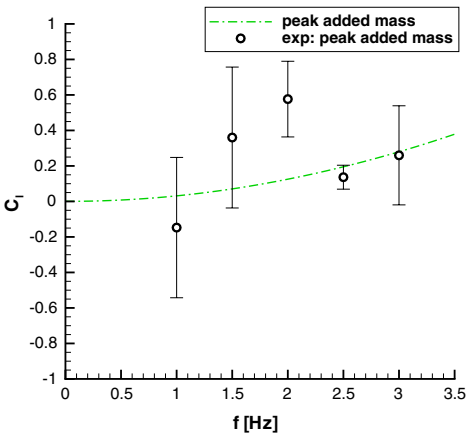

Fig. 5 Comparison of peak theoretical and measured added-mass contributions; theoretical values derived from Theodorson (1935)

In Fig. 5, the peak experimental added-mass contribution is compared with the prediction from Theodorsen's non-circulatory theory for cases of sinusoidal plunging. Despite the large variation associated with the measurements, the discrepancy between experiment and theory is pronounced, particularly at a plunge frequency of 2 Hz. When examining the flow field for such cases, clearly defined vortical structures are shed from both leading and trailing edges, as shown in the visualization of Fig. 6. These vortices, analogous to the structures found by Ringuette et al. (2007), in turn induce strong forces on the airfoil, which cannot be accounted for with Theodorson's inviscid theory.

Based on this result, it becomes clear that direct force measurements of such unsteady aerodynamic cases are limited in their accuracy since the separation of the circulatory and non-circulatory components from the inertial

Fig. 4 SD7003 carbon-fibre profile and dummy cylinder shown for comparison; note cylinder identical to profile in mass (±0.5 g) and spanwise distribution

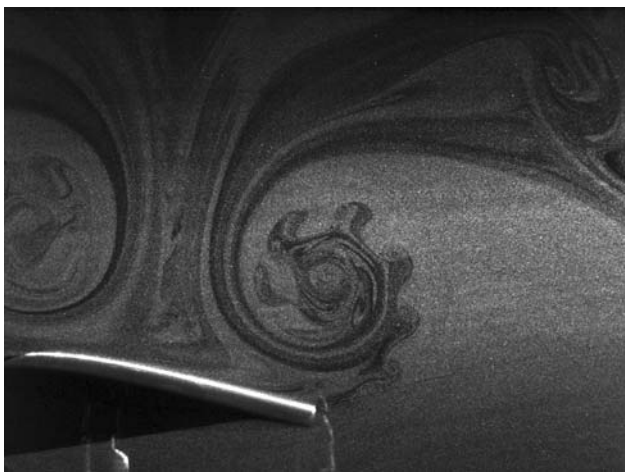

Fig. 6 Visualization depicting strong leading- and trailing-edge separation at bottom of stroke during a dynamic-tare measurement

component during the dynamic-tare cannot be performed. To confound the measurements even further, the inertial forces grow rapidly with f^2 such that at $k = 0.25$ they are approximately an order-of-magnitude larger than the aerodynamic forces, thus further deteriorating the accuracy of the measurements. In fact, for this range of reduced frequencies, the measurement error grows inversely proportional with $k^2 \propto (f/U_\infty)^2$ since the aerodynamic and inertial forces are proportional to U_∞^2 and f^2, respectively. Therefore in this investigation accurate direct force measurements were not possible. Rather the authors concentrated on PIV measurements to better understand the LEV formation process. These results will be presented in the following section.

5 Results

5.1 Reference (sinusoidal) case

Pure-plunging motions were selected for this study since the effective angle of attack distributions for such cases remain constant over the airfoil chord. This is possible since the introduction of relative leading- and trailing-edge velocities based on rotation (known as the dynamic-cambering effect) have been avoided. In Fig. 7, plots of dimensionless vorticity for 12 individual phases over the cycle are shown, where $t/T = 0$ corresponds to the top of the stroke. One can identify the clear evolution of the LEV over the downstroke, with first signs of a LEV at $t/T = 0.167$. The LEV subsequently grows in size and strength culminating in a large vortex on the order of the airfoil chord at $t/T = 0.333$. Only after this point does the separation open and vortex pinch-off occur. During the LEV formation process lift continuously increases beyond the peak static-stall value, as described in McCroskey (1982), and thus nearly continuous counter-clockwise vorticity, defined in this study as being negative, is shed from the trailing edge. This feature can be explained through Kelvin's law:

$$\frac{D\Gamma}{Dt} = 0, \tag{8}$$

such that the flux of counter-clockwise (negative) vorticity convected from the airfoil trailing edge is equal to the rate at which circulation of the leading-edge vortex grows with time:

$$\frac{D\Gamma_{\mathrm{LEV}}}{Dt} = u_{\mathrm{conv}} \int_s \omega_z \mathrm{d}s, \tag{9}$$

where s is a control surface placed normal to the freestream direction at the trailing edge. Just before the airfoil reaches the bottom of the stroke at $t/T = 0.417$, the strong counter-rotating vorticity shed at the trailing edge begins to roll-up into a trailing-edge vortex (TEV) due to the apparent interaction with the LEV passing overhead. This TEV grows very rapidly in strength and cuts apart the original LEV from the separated region above the airfoil, distinctly seen at the bottom of the stroke ($t/T = 0.5$). Thereafter the vortex pair (mushroom structure) convect rapidly downstream and the flow reattaches over the airfoil, moving from the leading edge back towards the trailing edge. By the time the airfoil reaches the middle of the upstroke ($t/T = 0.75$), the flow is again fully attached and a shear layer characteristic of static conditions is emitted from the trailing edge. As the airfoil approaches the top of the stroke a clear and repeatable instability is found in the wake such that even after 100 cycles of averaging the approximate alternating vortex position is the same, suggesting that the onset of this instability is forced by the motion and is not merely stochastic.

5.2 Effect of kinematics on LEV formation

When examining the effective angle-of-attack distribution for the various cases in Fig. 2, one can observe that the asymmetric and fast-sinusoidal cases pass through the static-stall angle at a much steeper rate when compared to the sinusoidal and peak-shifted cases. This has the effect of strengthening the shear layer feeding the LEV earlier on in the downstroke. Conversely for the peak-shifted case, the feeding only reaches its full strength in the second half of the downstroke. This variation is clearly visible when comparing the development of the LEV over the downstroke at $t/T = 0.25$ ($t/T = 0.333$ for the fast-sinusoidal case) as shown in Fig. 8.

When comparing Fig. 8b, d, one finds that the LEVs are nearly identical, albeit the asymmetric case has a more concentrated and symmetric core. The strength and shape of the planar wake are also very similar. The cause for difference between the two cases lies in the history effects, i.e. the state of the boundary layer and the surrounding flowfield at the beginning of the downstroke. At this phase ($t/T = 0$), the flow has relaxed to a quasi-steady condition for the asymmetric case since the upstroke is relatively slow ($f = 2$ Hz), whereas for the fast-sinusoidal case the boundary-layer is locally separated and the shear layer is much thicker. The comparison of the starting conditions ($t/T = 0$) in the LEV formation process for these two cases is shown in Fig. 9.

5.3 Effect of kinematics on wake formation

At a later stage in the cycle corresponding to $t/T = 0.5$, when the sinusoidal and peak-shifted cases are at the bottom of the stroke ($t/T = 0.667$ for the fast-sinusoidal case),

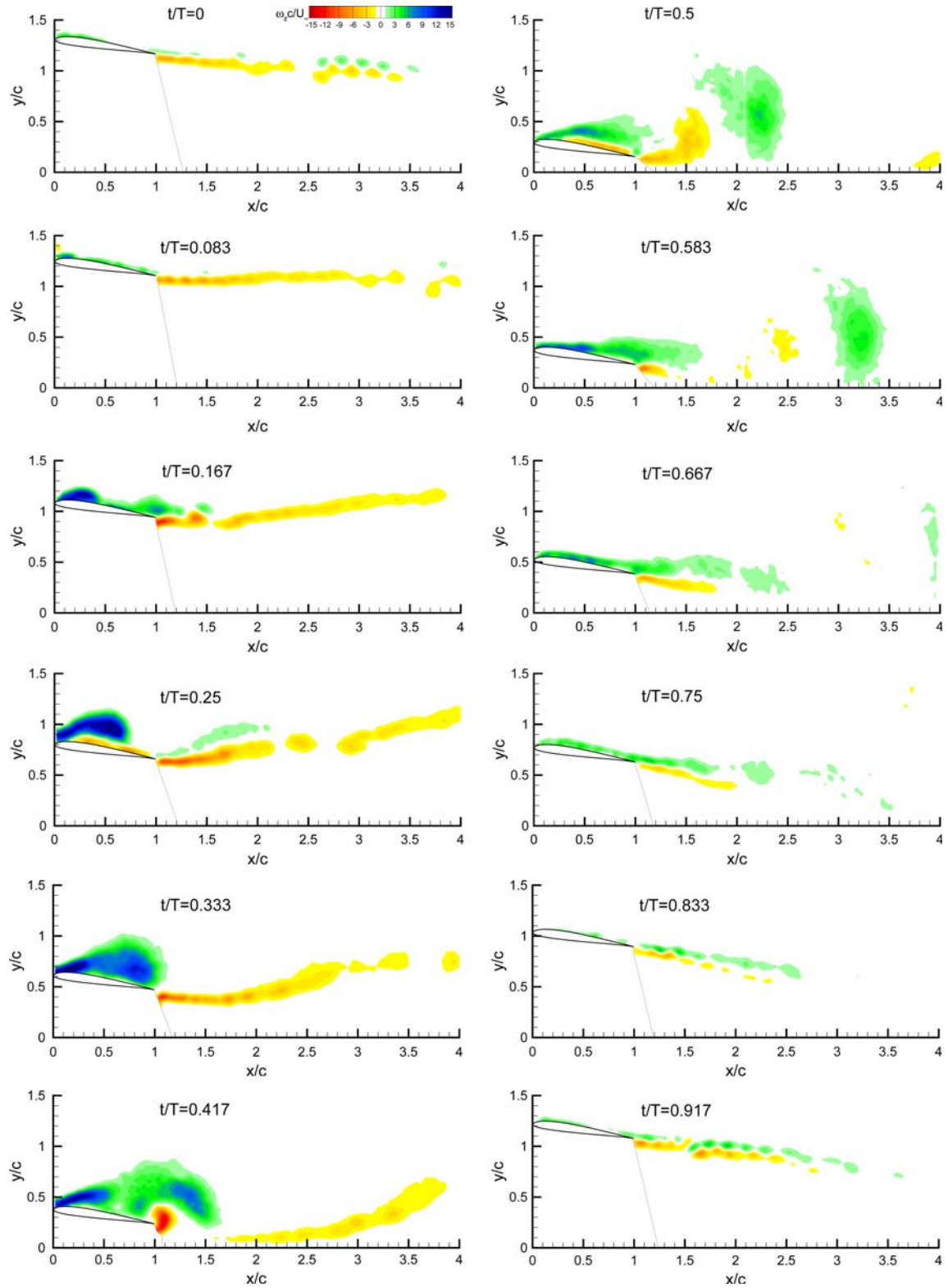

Fig. 7 Plots of dimensionless vorticity for the reference case, a sinusoidal plunging motion with a mean angle of attack of $\alpha_o = 8°$; note masking under airfoil necessary due to reflections and shadow effects

the LEV–TEV vortex pair has now begun its convection downstream. The comparison of the vortex positioning amongst the various cases is shown in Fig. 10. Again it is found that those cases with an earlier LEV formation onset time, associated with a steeper rise in the effective angle of attack slope, are also more advanced in the wake. This

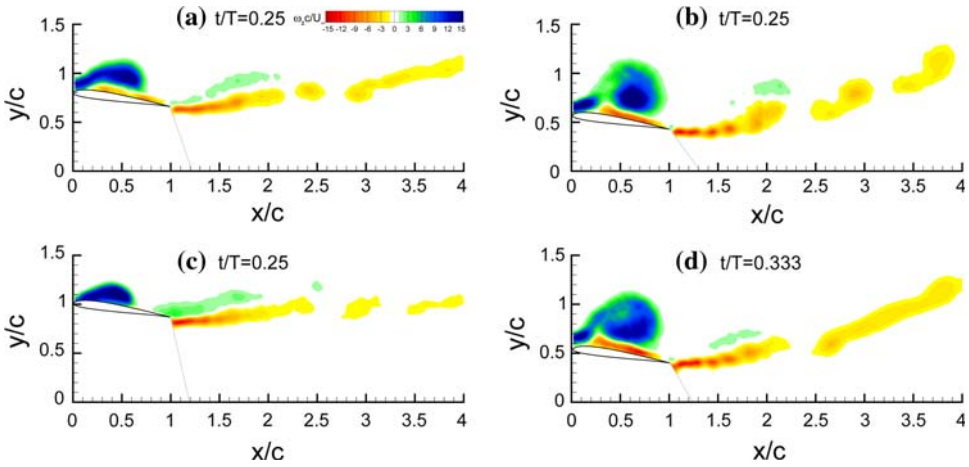

Fig. 8 Plots of dimensionless vorticity during the downstroke ($t/T = 0.25$) for **a** sinusoidal, **b** asymmetric, **c** peak-shifted and **d** fast-sinusoidal cases; note $t/T = 0.333$ used for fast-sinusoidal case to compare equivalent LEV development time

suggests that the time from onset of formation to pinch-off does not vary dramatically amongst the various cases. For the two analogous cases (Fig. 10b, d) the difference in the wakes varies very little; in both cases, the LEVs are stretched vertically and the TEVs are broken up. The peak-shifted case (Fig. 10c), as before, is much younger in its development such that the TEV has yet to pinch-off from the trailing edge. In fact, the flow at this instant shares a resemblance with the sinusoidal case but at an earlier time step ($t/T = 0.417$), as shown in Fig. 7. Thus one can infer that the timing as well as the rate at which the given motion crosses the static-stall angle is of primary importance in the LEV formation process. However, the specific kinematics after the onset of LEV roll-up impact the relative timing of the pinch-off process and will be examined in the following section.

5.4 Vortex growth and pinch-off

By tracking the development of both the LEV and TEV in each frame and extracting the respective vortex circulation from the local vorticity field using Stokes' theorem:

$$\Gamma = \iint_A \omega_z \mathrm{d}A, \tag{10}$$

where the rectangular area A was selected in each time step to encompass the vortex of interest, the dimensionless circulation of both the LEV and TEV at each phase in the cycle could be determined.

In Fig. 11, the growth and decay periods of the respective LEVs and TEVs are shown for all four motions. The maximum circulation of the LEV associated with the last time step before vortex pinch-off and maximum lift augmentation is found to occur at $t/T = 0.333$ for the sinusoidal and asymmetric motions, whereas it occurs later for the peak-shifted and fast-sinusoidal motions at $t/T = 0.417$. When comparing this result to the position of maximum effective angle of attack in Fig. 2a one can infer that a peak-circulation lag ranging between approximately $30° \leq \varphi \leq 60°$ is present in all cases, where the fast-sinusoidal motion exhibits both the largest value of circulation and delay, as would be expected. Of significance is the occurrence in all cases of pinch-off before the airfoil reaches the bottom of the stroke at $t/T = 0.5$. However, both the asymmetric and corresponding fast-sinusoidal cases, and even more noticeably the peak-shifted case demonstrate a later pinch-off and thus superior performance when compared to the reference sinusoidal motion.

When comparing the LEV timing and growth rate for the various motions as a function of dimensionless time in Fig. 11b, one finds that the asymmetric and analogous fast-sinusoidal curves are nearly identical, albeit the fast-sinusoidal motion achieves a slightly higher peak value. This again strengthens the argument that history effects do not play a dominant role in the LEV formation process. Similarly, the sinusoidal and peak-shifted cases share nearly identical LEV onset and growth periods. However, the peak-shifted case, with its maximum feeding velocity

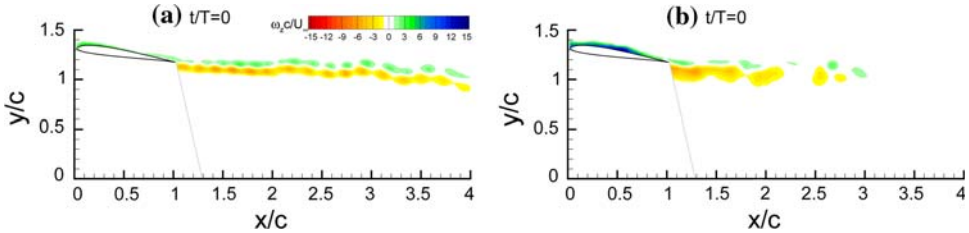

Fig. 9 Plots of dimensionless vorticity at top of stroke ($t/T = 0$) for **a** asymmetric and **b** fast-sinusoidal cases, demonstrating the importance of the history effects just before the LEV formation process begins

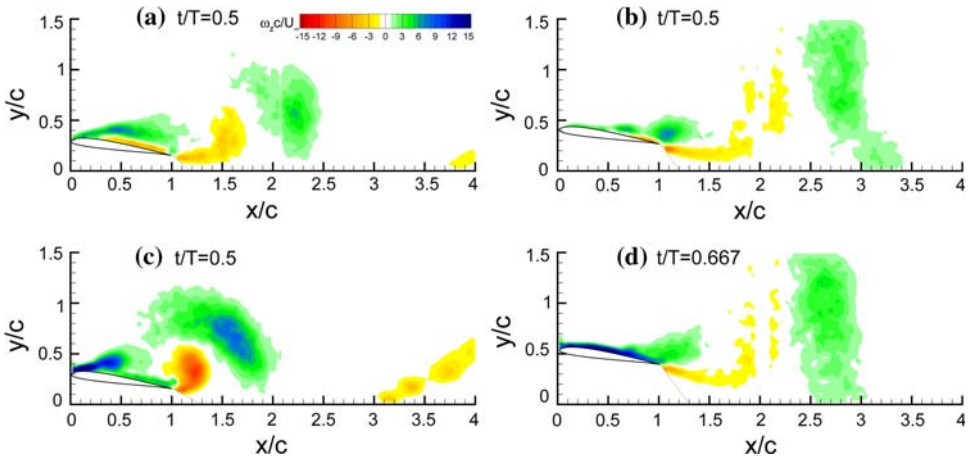

Fig. 10 Plots of dimensionless vorticity around bottom of stroke ($t/T = 0.5$) for **a** sinusoidal, **b** asymmetric, **c** peak-shifted and **d** fast-sinusoidal cases; note $t/T = 0.667$ used for fast-sinusoidal case to compare equivalent convection times of LEV and TEV in wake

occurring only later on in the downstroke, sustains LEV growth long after the sinusoidal motion's LEV has pinched-off. This is a dramatic result despite a relatively small increase in peak plunge velocity and energy expenditure.

In all cases, the TEV is found to form only once the corresponding LEV has reached its maximum strength and begins convecting downstream. In turn, the TEV rapidly loses strength in the wake due to interaction with the LEV. Again referring to Fig. 11b, one can identify that for the reference sinusoidal case the TEV forms relatively late and is weakest among the four motions. This effect can be substantiated through Kelvin's law (Eq. 8).

Based on the discussion in Sect. 2.2 regarding optimal vortex formation, the LEV and TEV formation times for the various test cases are presented in Fig. 12. When examining the peak formation time, known as the formation number, one can infer that all values reduce into a range of $4.4 < \hat{T} < 5.0$, agreeing well with the concept of an optimal vortex formation time presented by Dabiri (2009). This result suggests that in order to shed the LEV even later, i.e. at the bottom of the stroke, in order take full advantage of the dynamic-stall process, a more gradual feeding of the LEV would be necessary. This effect has been clearly demonstrated with the peak-shifted motion. However, the authors believe an additional pitching motion would be desirable late in the stroke to delay the pinch-off process even further.

5.5 Vortex convection

To complete the discussion, a study of the relative vortex positioning and convective velocity has been performed. The vortex trajectories were obtained by tracking the concentrated core whereas the convective velocities were based on a simple linear interpolation of the vortex positions with time. Shown in Figs. 13 and 14 are the respective vortex trajectories and convective velocities for both the LEVs and TEVs. In the case of the relative LEV

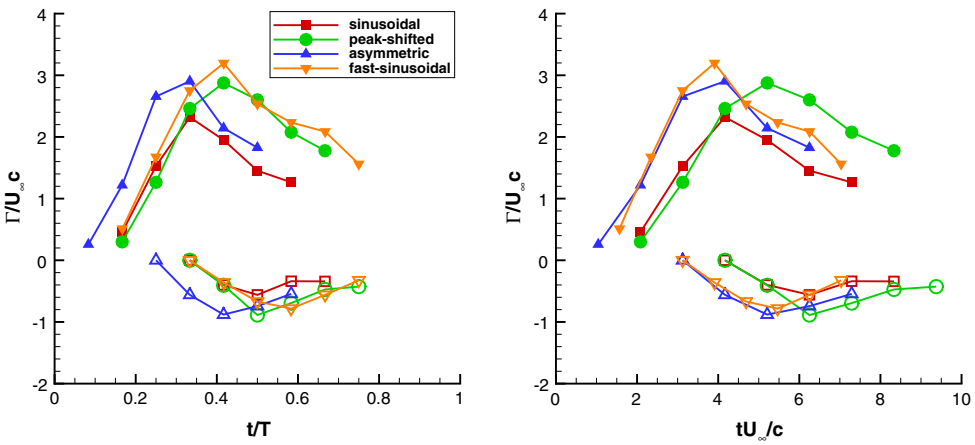

Fig. 11 Development of LEV and TEV circulation as a function of **a** period and **b** dimensionless time; note *solid* and *hollow symbols* represent LEVs and TEVs, respectively

(a) as a function of period **(b)** as a function of time

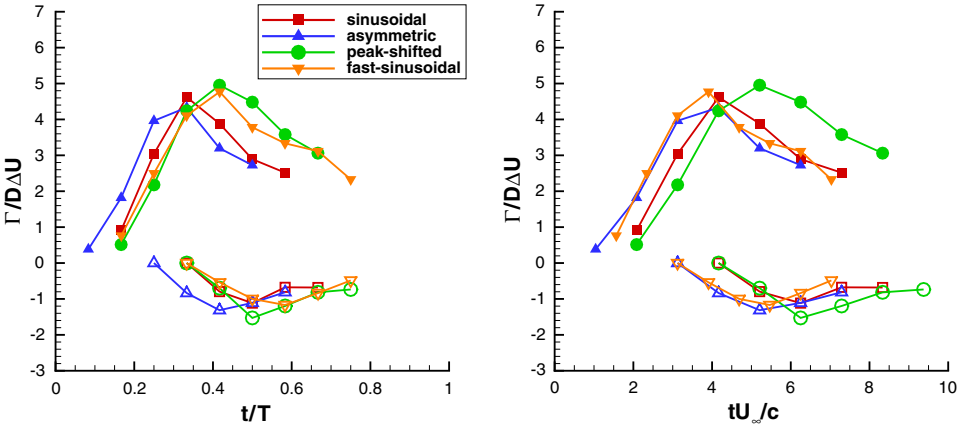

(a) as a function of period **(b)** as a function of time

Fig. 12 Formation time as a function of **a** period and **b** dimensionless time; note *solid* and *hollow symbols* represent LEVs and TEVs, respectively

position, as expected it follows the airfoil surface during the formation process. Once pinch-off takes place and the LEV convects into the wake, the vortex tends to follow a horizontal trajectory. The exception to this rule is found in the fast-sinusoidal case where the LEV shoots upwards and then later drifts back down. The corresponding TEV positions tend to curve slightly upwards for all cases due to the mutual induction of the vortex pair. The most drastic upwards movement corresponds to the TEV from the sinusoidal motion. In all cases, there exists a strong correlation between the LEV and TEV positions.

When examining the corresponding axial convection velocities, the LEV core is found to convect very slowly during the formation process but then accelerate rapidly once emitted into the wake. In fact a clear asymptotic behavior towards $u_{\text{conv}}/U_\infty = 1$ is visible in Fig. 14a. This result agrees well with the measurements made by Panda and Zaman (1994) for LEVs in the wake of a pitching airfoil. Again the fast-sinusoidal case shows exceptional variation in the wake attributed to the strong interaction with the TEV. For the TEV convection velocities shown in Fig. 14b, again a clear asymptotic behavior is visible, whereby the TEV for the sinusoidal motion breaks-up rapidly as can be seen in Fig. 7 between time steps $t/T = 0.583$ and $t/T = 0.667$. Despite this outlier, it can be generalized that all vortex convection velocities approach the freestream velocity asymptotically within two chord-lengths of the trailing edge.

6 Conclusions

An investigation into the formation of LEVs for various plunging kinematics has been performed using PIV. First, a discussion on the decomposition of aerodynamic loads into circulatory and non-circulatory components is treated and compared with dynamic tares in the wind tunnel. This section demonstrates the limitations associated with the separation of inertial and aerodynamic forces through the dynamic-tare method. Subsequently the evolution of the LEV for a reference (sinusoidal) motion is examined in detail. When compared to this reference case, asymmetric and peak-shifted motions are found to impact the onset and growth in the LEV formation process. Most promising was the delayed growth and pinch-off for the peak-shifted case where the LEV convected from the airfoil just before the bottom of the stroke. When examining the growth in circulation during the LEV formation process, it was found

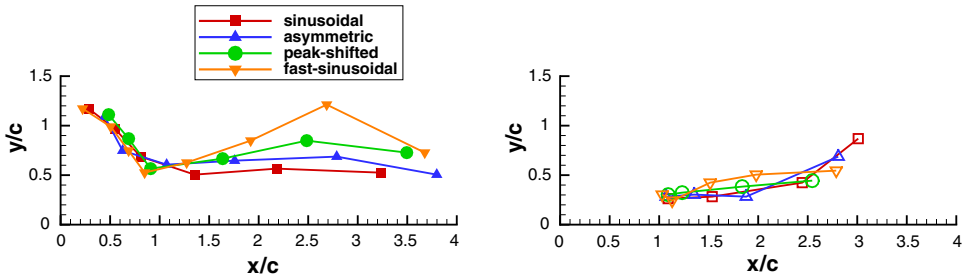

(a) LEV position **(b)** TEV position

Fig. 13 Trajectories of LEV and TEV cores for the four test cases

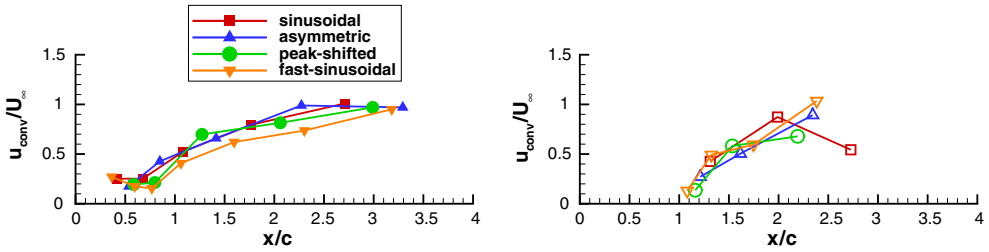

Fig. 14 Convection velocities of LEV and TEV cores for the four test cases: **a** LEV convection velocity, **b** TEV convection velocity

that all motions exhibited vortex pinch-off within $4.4 < \hat{T} < 5.0$, agreeing well with the concept of optimal vortex formation. This suggests that by carefully tuning the airfoil kinematics, thus gradually feeding the LEV over the downstroke, it is to some extent possible to stabilize the LEV without the necessity of a spanwise flow.

Acknowledgments The authors would like to thank Dr. Michael Ol from Wright-Patterson AFB for the fruitful discussions regarding Theodorsen's theory. This research was supported by the Deutsche Forschungsgemeinschaft (DFG) within the national priority program entitled *Nature-Inspired Fluid Mechanics* (SPP1207).

References

Dabiri JO (2009) Optimal vortex formation as a unifying principle in biological propulsion. Ann Rev Fluid Mech (online) 41:17–33

Ellington CP (1999) The novel aerodynamics of insect flight: applications to micro-air vehicles. J Exp Biol 202:3439–3448

Kuessner HG (1936) Zusammenfassender bericht ueber den instationaeren auftrieb von fluegeln. Luftfahrtforschung 13:410–424

Lian Y, Ol MV, Shyy W (2008) Comparative study of pitch-plunge airfoil aerodynamics at transitional reynolds number. 46th AIAA aerospace sciences meeting and exhibit, AIAA-2008-652-812, Reno, USA

McCroskey WJ (1982) Unsteady airfoils. Ann Rev Fluid Mech 14:285–311

Milano M, Gharib M (2005) Uncovering the physics of flapping flat plates with artificial evolution. J Fluid Mech 534:403–409

Mueller TJ, Batill SM (1982) Experimental studies of separation on a two-dimensional airfoil at low reynolds numbers. AIAA Journal 20 No. 4:457–463

Nerger D, Kaehler CJ, Radespiel R (2003) Zeitaufgeloeste pivmessungen an einem schwingenden sd7003-profil bei re=60000. 11 GALA Fachtagung, Braunschweig, Germany

Ohmi K, Coutanceau M, Loc TP, Dulieu A (1990) Vortex formation around an oscillating and translating airfoil at large incidences. J Fluid Mech 211:37–60

Ol MV, McAuliffe BR, Hanff ES, Scholz U, Kaehler C (2005) Comparison of laminar separation bubble measurements on a low reynolds number airfoil in three facilities. 35th AIAA fluid dynamics conference and exhibit, AIAA-2005-5149, Toronto, Canada

Panda J, Zaman KBMQ (1994) Experimental investigation of the flow field on an oscillating airfoil and estimation of lift from wake surveys. J Fluid Mech 265:65–95

Ringuette MJ, Milano M, Gharib M (2007) Role of the tip vortex in the force generation of low-aspect-ratio normal flat plates. J Fluid Mech 581:453–468

Rival D, Tropea C (2009) Characteristics of pitching and plunging airfoils under dynamic-stall conditions. 47th AIAA aerospace sciences meeting and exhibit, AIAA-2009-0537, Orlando, USA

Selig M, Guglielmo J, Broeren A, Giguere P (1995) Summary of low-speed airfoil data. SoarTech Publications, Virginia Beach, USA

Theodorsen T (1935) General theory of aerodynamic instability and the mechanisms of flutter. NACA Report No 496

Thomas ALR, Taylor GK, Srygley RB, Nudds RL, Bomphrey RJ (2004) Dragonfly flight: Free-flight and tethered flow visualizations reveal a diverse array of unsteady lift-generating mechanisms, controlled primarily via angle of attack. J Exp Biol 207:4299–4323